Thermo-elastic response of monolithic and composite plates to a thermal shock

J.M. Lefeuvre [1], D.C. Dunand *

Department of Materials Science and Engineering, Massachusetts Institute of Technology, Cambridge, MA 02139, USA

Abstract

The thermo-mechanical behavior of thin plates subjected to a step-shaped heat flux is studied analytically and experimentally. First, closed-form solutions for temperature and curvature as a function of time are derived for orthotropic monolithic plates. Second, composite plates are modeled by using equivalent properties and by taking into account a non-uniform fiber distribution, which leads to a bilayer effect. Finally, experimental temperature and curvature measurements on unreinforced Ti–6Al–4V plates and Ti–6Al–4V plates reinforced with unidirectional SiC fibers are compared to these analytical predictions. © 1999 Elsevier Science Ltd. All rights reserved.

Keywords: Thermal shock; Thermoelasticity; Curvature; Plates; Titanium; Metal matrix composite

1. Introduction

Because monolithic and fiber-reinforced titanium alloys exhibit outstanding specific mechanical properties at room and elevated temperatures, they are very attractive for aeronautical structures subjected to severe thermomechanical conditions. During atmospheric reentry or high acceleration, external structures are subjected to a thermal shock by aerofriction resulting in a rapid surface temperature increase and a concomitant high thermal gradient from the surface. The temperature distribution within the structure dictates its thermal expansion and the resulting deformation,

usually described as curvature for flat structures such as skins, foils or sheets. Unlike a monolithic plate, a heterogeneous plate subjected to a uniform, time-independent temperature exhibits internal stresses and curvature, as first analyzed by Stoney (1909) for the simple case of a bilayer material. Recently, Suresh and co-workers (e.g. Suresh et al., 1994; Finot et al., 1996; Finot and Suresh, 1996) examined the general case of multilayered or functionally graded materials. They derived the curvature and internal stresses of a plate deforming elastically or plastically, and also considered the case of large deformations. Their work included experimental results as well as analytical and numerical solutions. While a uniform thermal gradient in a monolithic material induces a curvature without internal stresses (Timoshenko and Goodier, 1970), the case of a composite is more complex. The time-independent problem was analyzed by Aboudi et al. (1994, 1997) for fiber-reinforced composites and functionally graded

---

* Corresponding author. Present address: Department of Materials Science and Engineering, Northwestern University, Evanston, IL 60208, USA. E-mail: dunand@nwu.edu.
[1] Present address: Centre de Recherches et d'Etudes d'Arcueil, 94114 Arcueil, France.

composites. These authors found that standard homogenization schemes produce questionable results, especially in the case of a low number of fiber rows with large-diameter fibers, and developed an explicitly coupled analysis to determine moments induced by a thermal gradient for a constrained plate.

The problem of thermal shock in composite plates has been addressed by Mukherjee and Sinha (1996) who performed a finite-element analysis and investigated various thermo-mechanical variables as a function of time. In the present article, we consider the case of a plate subjected to a step-shaped heat flux with convection occurring on both sides of the plate. This definition of thermal shock is different from that used by other authors, but allows comparison with simple experiments and is close to conditions encountered in aerospace structures. We first develop an analytical model giving closed-form solutions for the time-dependence of the temperature and the curvature of a monolithic plate. We then extend the model to the case of a composite exhibiting a non-uniform fiber volume fraction. In the case where the distribution of the fibers within the thickness of the plate is slightly asymmetric, we suggest that equivalent homogeneous properties of the composite can be used, provided one takes into account a bilayer effect. Experimental results for both monolithic Ti–6Al–4V and composite Ti–6Al–4V/SiC plates are compared to the theoretical analysis.

2. Theory

2.1. Homogeneous plate

We consider the thermo-mechanical response of an unconstrained, infinite, orthotropic plate of thickness e subjected to a thermal shock at time $t = 0$, consisting of a constant heat flux H on one of the plate sides with convection on both its sides Fig. 1. The plate is characterized by a through-thickness (in the x-direction) thermal diffusivity δ, a through-thickness thermal conductivity κ, in-plane Young's moduli E_y and E_z, a Poisson's ratio v_{yz}, and in-plane coefficients of thermal expansion
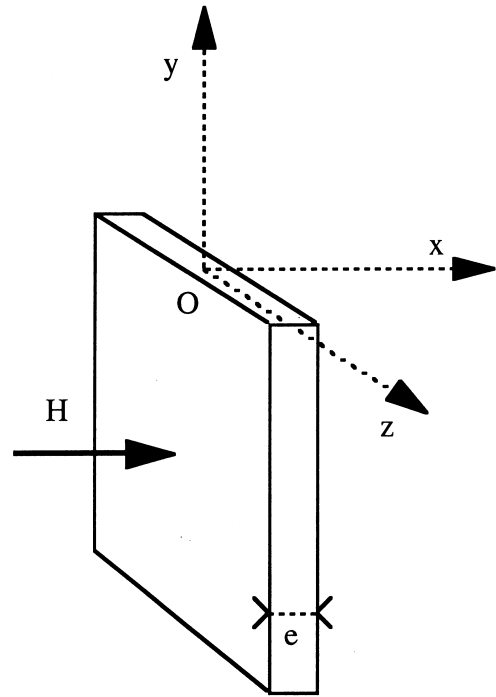

Fig. 1. Isotropic plate subjected to a thermal flux H.

α_y and α_z. Convection is assumed to take place with an environment at constant temperature T_0, with coefficients of convection h_1 and h_2 on the heated and unheated side, respectively. All the material properties are assumed temperature-independent.

Assuming that at all times, the plate is at mechanical equilibrium and that the deformation of the plate is small, the thermal problem can be solved independently of the mechanical response, which can then be determined.

2.1.1. Thermal problem

We seek to determine the temperature $T(x,t)$ as a function of time t and of the position x within the plate thickness, neglecting edge effects. The function $T(x,t)$ satisfies the Laplace equation with the boundary conditions given above:

$$\frac{\partial^2 T}{\partial x^2} = \frac{1}{\delta}\frac{\partial T}{\partial t} \quad \text{for} \quad -\frac{e}{2} < x < \frac{e}{2}, \tag{1a}$$

$$T = T_0 \quad \text{for} \quad -\frac{e}{2} < x < \frac{e}{2} \text{ and } t = 0, \tag{1b}$$

$$-\kappa \frac{\partial T}{\partial x} + h_1(T - T_0) = H \text{ for } x = -\frac{e}{2} \text{ and } t > 0,$$

(1c)

$$-\kappa \frac{\partial T}{\partial x} - h_2(T - T_0) = 0 \text{ for } x = \frac{e}{2} \text{ and } t > 0.$$

(1d)

After modifying system (1a)–(1d) as shown in Appendix A, it can be solved as in Ozisik (1993) by separation of variables, leading to

$$T = a + b\left(x + \frac{e}{2}\right) + \sum_m c_m \left[\beta_m \cos\left(\beta_m\left(x + \frac{e}{2}\right)\right)\right.$$
$$\left. + \frac{h_1}{\kappa} \sin\left(\beta_m\left(x + \frac{e}{2}\right)\right)\right] \exp[-\delta\beta_m^2 t],$$

(2)

where the coefficients a, b, c_m and β_m are given in Appendix A.

The average temperature $\overline{T}$ is defined as

$$\overline{T} = \frac{1}{e} \int_{-e/2}^{e/2} T(x) \, dx.$$

(3)

If the plate thickness e is small, the temperature T can be assumed to be uniform. The average temperature can be found by writing an energy balance:

$$\frac{\kappa}{\delta} e \frac{d\overline{T}}{dt} = H - (h_1 + h_2)(\overline{T} - T_0)$$

(4)

the solution of which is

$$\overline{T}(t) = T_0 + \frac{H}{h_1 + h_2}\left(1 - e^{-\delta(h_1+h_2)t/\kappa e}\right).$$

(5)

From Eq. (5), $\overline{T}$ is found to increase at $t = 0$ with the following rate:

$$\dot{\overline{T}}_0 = \frac{d\overline{T}}{dt}\bigg|_{t=0} = \frac{\delta H}{e\kappa}$$

(6)

and to tend to a limiting value for large times given by

$$\overline{T}_\infty = \overline{T}_{|t\to\infty} = T_0 + \frac{H}{h_1 + h_2}.$$

(7)

The thermal gradient can be determined as the first derivative of Eq. (2). The average thermal gradient is directly expressed as

$$\overline{\frac{\partial T}{\partial x}} = \frac{1}{e} \int_{x=-e/2}^{x=e/2} \frac{\partial T}{\partial x} \, dx = \frac{1}{e} T\big|_{x=-e/2}^{x=e/2}.$$

(8)

It tends to the following limiting value:

$$\frac{\overline{\partial T}}{\partial x}\bigg|_{t\to\infty} = \frac{1}{e} T_{|t\to\infty}\big|_{x=-e/2}^{x=e/2} = \frac{1}{e}[(a + be) - (a)] = b$$
$$= -H \frac{h_2}{\kappa(h_1 + h_2) + h_1 h_2 e}.$$

(9a)

Again, assuming that the plate thickness e is small, the average thermal gradient can be approximated by

$$\frac{\overline{\partial T}}{\partial x}\bigg|_{t\to\infty} = -\frac{H}{\kappa} \frac{h_2}{h_1 + h_2}.$$

(9b)

In conclusion, the evolution of the temperature field can be described by the average temperature, given by Eq. (5), and the average thermal gradient, which tends to the value given in Eq. (9b).

2.1.2. Mechanical problem

We seek to determine the deformation and the stresses induced in the plate by a temperature profile $T(x,t)$ assuming that (i) the plate is flat at temperature T_0, (ii) the plate is unconstrained, (iii) plane stress conditions can be used because the thickness of the plate is small, (iv) the elastic problem can be solved with the theory of small deformations. Similar problems are addressed in Timoshenko and Woinowsky-Krieger (1959), where the deformation of the plate is described by the following main strains ε_y and ε_z, in the y and z directions, respectively:

$$\varepsilon_y = \varepsilon_{y0} + \rho_y x,$$

(10a)

$$\varepsilon_z = \varepsilon_{z0} + \rho_z x,$$

(10b)

where ε_{y0} and ε_{z0} are the average main strains and ρ_y and ρ_z are the main curvatures. Since all the results are symmetrical with respect to the axis y and z, they are written in a compact manner with both indices separated by a comma. Eqs. (10a) and (10b) are then expressed as

$$\varepsilon_{y,z} = \varepsilon_{y0,z0} + \rho_{y,z} x.$$

(10c)

The average strains and curvatures are determined by writing the elastic relations:

$$\varepsilon_{y,z} = \frac{\sigma_{y,z}}{E_{y,z}} - v_{zy,yz}\frac{\sigma_{z,y}}{E_{z,y}} + \alpha_{y,z}(T - T_0), \tag{11}$$

where σ_y and σ_z are the main stresses and the orthotropic relation holds:

$$v_{yz}E_z = v_{zy}E_y. \tag{12}$$

Eq. (11) can be inverted:

$$\sigma_{y,z} = \frac{E_{y,z}}{1 - v_{yz}v_{zy}}\big[(\varepsilon_{y,z} - \alpha_{y,z}(T - T_0)) \\ + v_{zy,yz}(\varepsilon_{z,y} - \alpha_{z,y}(T - T_0))\big]. \tag{13}$$

Average strains can be found by introducing Eq. (13) into the force equilibrium equation (as the plate is unconstrained):

$$\int_{-e/2}^{e/2} \sigma_{y,z}(x)\,\mathrm{d}x = 0 \tag{14}$$

to yield a linear system of two equations with two unknowns $u_{y,z}$:

$$u_{y,z} = \int_{-e/2}^{e/2} [\varepsilon_{y,z} - \alpha_{y,z}(T - T_0)]\,\mathrm{d}x. \tag{15}$$

The determinant of Eq. (14) is zero only if

$$v_{yz} = \frac{1}{v_{zy}} \tag{16}$$

which is not physically possible, because the Poisson's ratio cannot exceed 1. So the two unknowns $u_{y,z}$ must be zero and Eq. (14) lead to

$$\varepsilon_{y0,z0} = \alpha_{y,z}\left(\frac{1}{e}\int_{-e/2}^{e/2} T(x)\,\mathrm{d}x - T_0\right). \tag{17}$$

So, the average strains depend on the increase of average temperature. Their time dependence is given by introducing Eq. (5) into Eq. (17). They are not coupled by mechanical properties, as opposed to the case of the average strains of a bilayer submitted to a change of temperature (see Finot and Suresh, 1996).

The main curvatures can be found by introducing Eq. (13) into the momentum equilibrium equation:

$$\int_{-e/2}^{e/2} x\sigma_{y,z}(x)\,\mathrm{d}x = 0. \tag{18}$$

As before, this is a linear system where the two unknowns must be zero, yielding expressions for the curvatures similar to those for the average strains Eq. (17):

$$\rho_{y,z} = \alpha_{y,z}\frac{12}{e^3}\int_{-e/2}^{e/2} xT(x)\,\mathrm{d}x. \tag{19}$$

As expected, Eq. (19) predicts no curvature for a spatially uniform temperature. These equations can be rewritten using the expression for the temperature profile given by Eq. (2):

$$\rho_{y,z} = \alpha_{y,z}\left\{b + \frac{12}{e^3}\sum_m c_m\left[\frac{2\kappa - h_1 e}{2\kappa\beta_m}\cos(\beta_m e)\right.\right. \\ \left. + \frac{\kappa\beta_m^2 e + 2h_1}{2\kappa\beta_m^2}\sin(\beta_m e) - \frac{\kappa\beta_m + h_1 e}{\kappa\beta_m^2}\right] \\ \left. \times \exp[-\delta\beta_m^2 t]\right\} \tag{20}$$

which yields the curvatures as a function of time. Here again, we find that the two main curvatures are not coupled by mechanical properties, as opposed to the case of the average strains of a bilayer submitted to a change of temperature (see Finot and Suresh, 1996).

An expression can be independently found for the time-derivative of the curvatures by differentiating Eq. (19), using Eq. (1a) and performing a partial integration:

$$\frac{\mathrm{d}\rho_{y,z}}{\mathrm{d}t} = \delta\frac{12}{e^3}\alpha_{y,z}\left[x\frac{\partial T}{\partial x} - T\right]_{-e/2}^{e/2}. \tag{21}$$

Using Eqs. (1b)–(1d), the initial curvature rates are

$$\dot{\rho}_{y0,z0} = \frac{\mathrm{d}\rho_{y,z}}{\mathrm{d}t}\bigg|_{t=0} = -\delta\frac{6}{e^2}\alpha_{y,z}\frac{H}{\kappa}. \tag{22}$$

Furthermore, the curvatures tend to limits $\alpha_{y,z}b$ at long times, as show by Eq. (20). Using

Eq. (9b), the following approximation for limiting curvatures is found for the case of a small thickness e:

$$\rho_{y\infty,z\infty} = \alpha_{y,z} \left. \frac{\overline{\partial T}}{\partial x} \right|_{t\to\infty} = -\frac{\alpha_{y,z}}{\kappa} H \frac{h_2}{h_1 + h_2}. \tag{23}$$

In summary, the deformation of a plate during a thermal shock can be described by average main strains, which are related to the increase of average temperature, and main curvatures, which are related to the temperature profile.

2.2. Composite plate

The simplest approach for adapting to an orthotropic composite plate the results derived above for an orthotropic monolithic plate is to introduce in the above equations the equivalent thermomechanical properties of the composite material. However, an additional effect appears if the composite exhibits an asymmetry in the volume fraction with respect to the y–z plane bisecting the plate. We analyze this effect in the case of a uniform temperature, and then in the case of a thermal shock.

2.2.1. Uniform temperature
If the composite exhibits an asymmetry in the fiber volume fraction with respect to the y–z plane bisecting the plate, the plate bends like a bilayer material when submitted to a uniform increase of temperature, unlike a monolithic or a balanced composite plates. For a bilayered plate consisting of two isotropic layers referred to as materials I and II, with thicknesses e^I and e^{II} and thermoelastic properties as before, the isotropic curvature due to a uniform increase of temperature from T_0 to $\overline{T}$ can be expressed as in Finot and Suresh (1996):

$$\rho = -\frac{6}{(e^I + e^{II})} \frac{\bar{e}(1 + \bar{e})^2}{\overline{E}\bar{e}^4 + 4\bar{e}^3 + 6\bar{e}^2 + 4\bar{e} + 1/\overline{E}}$$
$$\times (\alpha^I - \alpha^{II})\overline{T}, \tag{24a}$$

where

$$\bar{e} = \frac{e^I}{e^{II}}, \tag{24b}$$

$$\overline{E} = \frac{E^I}{1 - v^I} \frac{1 - v^{II}}{E^{II}}. \tag{24c}$$

For unidirectional fiber composites produced by hot-pressing of composite plies of fibers and foils, the volume fraction of fibers can vary slightly within the thickness of the plate. Also, the thickness of the matrix layer closest to the plate surface can vary on either face of the plate, because of post-fabrication polishing, machining or pickling. The composite plate is then asymmetric and bends even for a uniform temperature, as opposed to a homogeneous plate. Because the composite plate is orthotropic and not isotropic, its shape is defined by two different main curvatures, unlike an isotropic bilayer. We thus introduce two temperature curvature factors ρ_y^T and ρ_z^T which give the main curvatures of the plate (assumed to be flat at temperature T_0) when it is at temperature $\overline{T}$:

$$\rho_{y,z} = \rho_{y,z}^T (\overline{T} - T_0). \tag{25}$$

These factors which depend on the fiber distribution homogeneity, are difficult to predict directly from observation of the plate, but can be measured by imposing a uniform increase of temperature to the plate. As suggested by Eqs. (24a)–(24c) their importance increases as the plate becomes thinner, and as the thermal expansion mismatch between the fibers and the matrix increases.

2.2.2. Thermal shock
In the case of a thermal shock of a thin plate with small fiber volume fraction asymmetry is small, we assume that the only significant effect of this asymmetry is to add a contribution to the curvature of the composite plate, which can be related to the average temperature through Eq. (25). This is because the increase of average temperature is large compared to the difference of temperature of the two sides of the plate. Therefore, the main curvatures of the plate during the thermal shock can be written as

$$\rho_{y,z} = \rho_{y,z}^H Hr(t) + \rho_{y,z}^T (\overline{T}(t) - T_0). \tag{26}$$

In this expression, the first contribution is due to the non-uniformity of temperature within the thickness of the plate, like for a homogeneous

plate in Eq. (20). We have introduced flux curvature factors

$$\rho_{y,z}^{H} = \frac{\alpha_{y,z}}{\kappa} \qquad (27)$$

and a dimensionless function $r(t)$ which can be deduced from Eq. (20):

$$r(t) = \frac{\kappa h_2}{\kappa(h_1 + h_2) + h_1 h_2 e}$$
$$\times \left\{ 1 + \frac{12}{e^3 b} \sum_m c_m \left[\frac{2\kappa - h_1 e}{2\kappa\beta_m} \cos(\beta_m e) \right. \right.$$
$$+ \frac{\kappa\beta_m^2 e + 2h_1}{2\kappa\beta_m^2} \sin(\beta_m e) - \frac{\kappa\beta_m + h_1 e}{\kappa\beta_m^2} \right]$$
$$\left. \times \exp[-\delta\beta_m^2 t] \right\}. \qquad (28)$$

Flux curvature factors involve equivalent properties of the composite for thermal expansion and through thickness thermal conductivity. Those equivalent properties can be measured separately. The second contribution to the curvature is due to the geometric asymmetry of the plate, and is related to the average increase of temperature of the plate, given by Eq. (5). This contribution depends on temperature curvature factors ρ_y^T and ρ_z^T of the plate, which can also be measured. They constitute a property of the plate. With Eq. (26), and assuming as before that thickness e is small, the limiting curvatures can be expressed as

$$\rho_{y\infty, z\infty} = \rho_{y,z}^{H} H \frac{h_2}{h_1 + h_2} + \rho_{y,z}^{T}(\bar{T}_\infty - T_0). \qquad (29)$$

3. Experimental procedures

3.1. Thermal shock apparatus

An apparatus was constructed to measure the evolution with time of the curvature of a plate submitted to a thermal shock, defined as a sharp step of heat flux at time $t = 0$ (Eqs. (1a)–(1d)). The heat flux is provided by a radiative furnace consisting of a quartz lamp with maximum power of

1.2 kW positioned at the focal line of a semi-elliptic, water-cooled reflector; the sample is positioned near the other focal line where the reflected light is focused over the whole width of the sample. The other unheated side of the plate can be cooled by blowing air uniformly on its surface at a controlled speed. The set-up thus allows to control both heat flux on the heated side and convection on the unheated side of the plate.

The last few millimeters of the end of the plate are clamped between two insulating quartz plates. A laser beam is reflected from the polished, unheated side of the plate to an observation screen. As the heat flux is established, the curvature-induced deflection of the reflected laser spot is video-taped while the temperature is recorded with thin thermocouples embedded at the center of the plate width. After the experiment, the video-tape is examined frame by frame and the deflection of the laser spot is determined from a graduated scale as a function of time.

Fig. 2 shows a schematic of the apparatus. The laser beam is reflected on a mirror M, positioned so that the line PM of length h is perpendicular to the plate of length d. The laser beam is then reflected from point M′ on the polished plate to point N′ on the screen, positioned at a distance S from, and parallel to, the plate. Assuming a constant radius of curvature R for the plate (distance OP or OM′), we can write

$$d = h \tan\alpha,$$
$$d = R \sin\beta, \qquad (30)$$

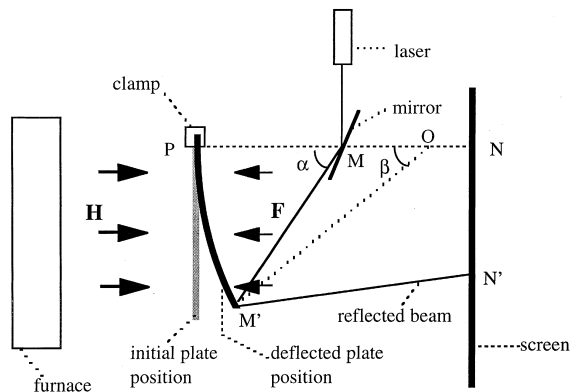Fig. 2. Schematic of experimental apparatus.

when the radius of curvature R is large enough.

The length NN′ on the scaled screen is

$$\text{NN}' = R\sin\beta + \tan(\alpha - 2\beta) \times (S - R(1 - \cos\beta)) \tag{31}$$

which can be approximated as

$$\text{NN}' = d\left(1 + \frac{S}{h}\right) - 2\frac{d}{R}\left(S\left(1 + \frac{d^2}{h^2}\right) + \frac{d^2}{h}\right) \tag{32}$$

if d is small compared to R. Defining the curvature ρ as the inverse of the radius of curvature R and the deflection D as the difference between the distance NN′ (for the heated, curved plate) and the distance NN'_0 (for the unheated, flat plate), Eq. (32) leads to

$$\rho = \frac{D}{2dS} \tag{33}$$

for h much larger than d (i.e. neglecting the terms d^2/Sh and d^2/h^2).

3.2. Samples

The samples were rectangular plates 70 mm long and 10 mm wide. For unreinforced samples, a rolled Ti–6Al–4V sheet (from Titanium and Alloys Corporation) of 1.6 mm thickness was used. Two types of composite samples were examined. First, samples B1–B5 (with 1.0 mm thickness) were processed by British Petroleum by liquid infiltration. They exhibited 35 vol% of Sigma SiC fibers (diameter 100 μm, from British Petroleum) and contained six plies. Second, samples M1–M10 were processed by Matra Défense (France) by plasma spraying and subsequent hot-pressing of single plies, containing SCS-6 SiC fibers (diameter 140 μm, from Textron). Samples M1–M5 (with 1.6 mm thickness) exhibited a volume fraction 30% and six plies, samples M6–M9 (with 1.2 mm thickness) a volume fraction 30% and five plies. Sample M10 (with 0.9 mm thickness) contained 35 vol% of Sigma SiC fibers and six plies.

The unheated side of the sample was polished with 1 μm diamond paste to maximize the reflection of the laser beam. The heated side of the sample was lightly ground and painted with a high emissivity, black paint (Tempil 2000 from Air Li-quide, baked near 250°C for about 2 h) to ensure that samples absorbed the heat flux from the furnace in a controlled, reproducible manner. To insulate the heated side of the plate from its unheated side, a light-weight frame of reflective aluminum foil was affixed around the plate with high-temperature glue, except for the clamped edge.

To determine the time-dependence of the average temperature, K-type thermocouples were introduced from the unheated side into one or several holes (1 mm in diameter and in depth) drilled in the thickness of the plate.

4. Results

4.1. Calibration

The heat flux H could be varied from 20 to 450 kW m^{-2} by varying the voltage applied to the lamp and the distance between sample and lamp. The step-shaped flux increase was achieved by first establishing a constant flux from the lamp and then rapidly removing a shutter shielding the sample. The absorbed heat was calibrated by recording the rise of temperature of a copper plate (with the same geometry as the investigated titanium samples and painted in a similar manner) insulated on all faces not exposed to the flux. Copper was chosen because of its high conductivity, leading to a uniform temperature within the sample. Within the first fifty degrees centigrade, the temperature rise was linear with time, and the heat flux H could be calculated from the slope T' of the curve, the thickness of the plate e, and the volumetric heat capacity of copper L ($L = 3.46 \times 10^6$ J K^{-1} m^{-3}):

$$H = T' \cdot L \cdot e. \tag{34}$$

Cooling was controlled through the velocity F of air blown on the sample, which was measured by a flowmeter giving the air flow Δ at room temperature and atmospheric pressure. Air was blown uniformly on the unheated surface of the sample with a tube drilled with holes at regular intervals of about 10 mm. The effective surface Σ subjected to the air flow was determined as 1000 mm^2 and the air velocity F was calculated as

Table 1
Properties of the layers of the bimetallic strip at 280°C used to compare the experimental (Exp) curvature ρ for a flux $H = 25$ kW m^{-2} and no active air cooling, and the theoretical curvature

	E (GPa)	α (10^{-6} K^{-1})	e (mm)	ρ (Exp) (m^{-1})	ρ (Eq. (24a)) (m^{-1})
Stainless steel	200	16	1	1.24	1.125
Aluminum	55	25	2		

$$F = \frac{\Delta}{\Sigma} \tag{35}$$

and could be varied from 0 to 2.00 ms^{-1}.

A control experiment for curvature measurements was performed on a bimetallic 10×70 mm^2 plate consisting of aluminum (constituent I) and stainless steel (constituent II) with a total thickness of 3 mm. This bimetallic strip was tested at low heat fluxes with negligible temperature gradients, so that the observed curvatures were due only to the average temperature. The deflection D of the laser beam was a linear function of the distance d from the clamp, thus confirming that the curvature was constant within the plate. Furthermore, the curvature induced by a change of temperature measured with a thermocouple, as calculated with Eq. (24a) matched well the experimentally measured curvature, as shown in Table 1 which also lists the materials properties used.

4.2. Thermal measurements

The temperature was measured with a single thermocouple embedded in the sample about 50 mm from the clamp. Without active cooling ($F = 0$), the temperature measurement was very reproducible. When active air cooling was used, careful placement of the thermocouple was necessary to avoid convective cooling of the thermocouple tip (the sides of the hole were filled with ceramic insulation). Temperature homogeneity was verified by measuring the limit temperature reached within a plate of Ti–6Al–4V under two different sets of conditions, as shown in Fig. 3 for a typical measurement. This figure shows that at distances more than 10 mm from the clamp, the temperature is nearly constant. On the other hand, a temperature drop was observed close to the clamp, indicating that significant heat losses occurred by conduction to the small unheated part of
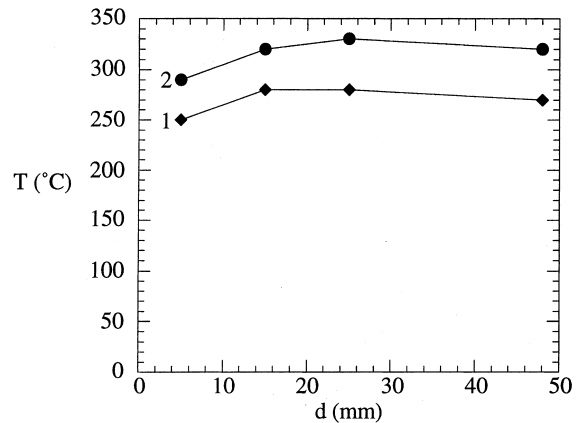

Fig. 3. Limiting temperature T as a function of the distance from the clamp d, for case 1 ($H = 25$ kW m^{-2}, $F = 0$) and case 2 ($H = 200$ kW m^{-2}, $F = 2.00$ m s^{-1}).

the plate in the clamp, to the quartz plates and to the clamp itself. It is expected that the thermal gradient and the associated sample curvature were also affected by this edge effect.

To determine the coefficients of convection on the heated and the non-heated faces, respectively, h_1 and h_2, a few experiments were carried out with a small heat flux ($H = 25$ kW m^{-2}) and various cooling velocities. With no active cooling ($F = 0$), for which convection was assumed to be the same on both sides of the sample, the experimental limiting temperature measured at about 50 mm from the clamp gives the coefficient of convection h_1 by using Eq. (7). Using the same flux, experiments were performed with active cooling. Assuming that convection on the heated side took place according to the case of no active cooling, the measured temperature yielded the coefficient of convection h_2 as a function of the cooling velocity F, using Eq. (7). The results for h_2 are presented in Fig. 4 h_1 corresponding to h_2 for no cooling. For a range of heat fluxes H from 25 to 300 kW m^{-2}, the
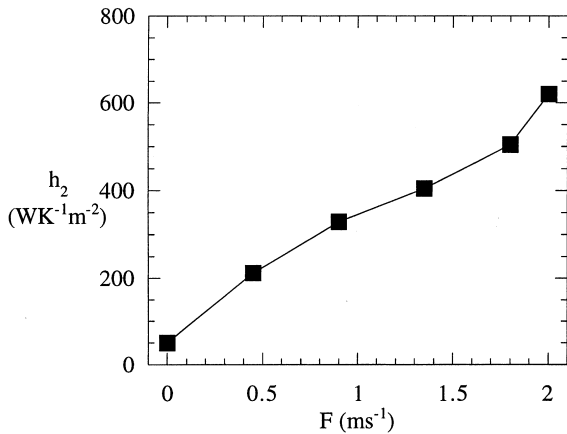
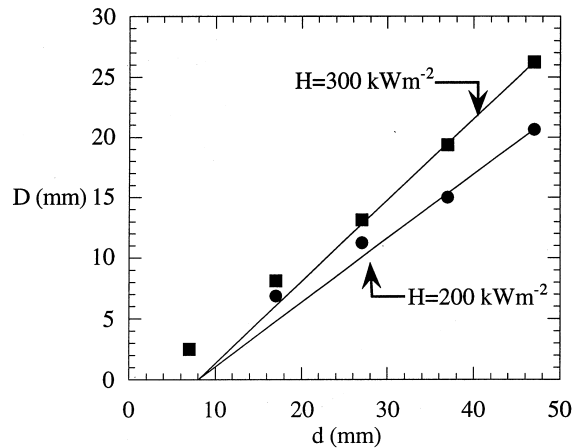Fig. 4. Coefficient of convection h_2 as a function of the cooling velocity F.

Fig. 5. Limiting deflection of the laser beam D as a function of the distance from the clamp d for a cooling velocity $F = 2.00$ m s^{-1}.

flux did not affect significantly the coefficient of convection, which was found to vary by less than 30 W m^{-2} K^{-1} (10%) within the temperature range 30–500°C. Moreover, it was found that the coefficients of convection were also nearly indistinguishable between monolithic plates, composite plates and bimetallic strip. This is expected since these coefficients are a surface property, and since all the metallic samples had surfaces with the same flat and polished finish aspect, with or without paint.

4.3. Monolithic Ti–6Al–4V plates

The curvature and average temperature induced by a step-shaped heat flux were measured for various heat fluxes H and cooling velocities F. The limiting curvature, which was reached within a few seconds (typically less than 10 s) was investigated first. The deflection of the laser beam at different points along the sample (different PM′ values, Fig. 2) was determined for a screen-specimen distance $S = 1.45$ m, as shown in Fig. 5. The deflection was not linear close to the clamp, indicating a reduced curvature. Extrapolation of the linear portion of the curve in Fig. 5 gives a y-axis intercept $y_0 = 8$ mm. All other measurements were then performed at a large distance from the clamp ($d = 47$ mm), replacing d in Eq. (33) with $d - y_0$, which yields

$$\rho = \frac{D}{2(d - y_0)S}. \tag{36}$$

Table 3 lists the limiting curvatures measured under various conditions.

Fig. 6 shows curvature and average temperature of a plate subjected to a step-shaped flux of 12 s. duration. A very sharp increase of curvature is observed at the beginning of the experiment and the final curvature is reached quickly, in contrast to the temperature which increases in a much smoother manner and does not reach its limiting
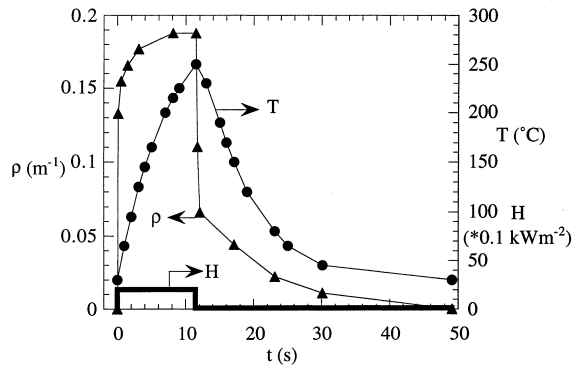

Fig. 6. Time-dependence of flux H, average temperature T and curvature ρ for a Ti–6Al–4V plate subjected to a thermal shock of 12 s duration, with a cooling velocity $F = 2.00$ m s^{-1} and a heat flux $H = 200$ kW m^{-2}.

value ($\bar{T}_\infty = 330°C$ for these conditions) before the flux is interrupted. The curvature is then recovered very quickly, confirming that the deformation is purely elastic. Again, the temperature decreases much more gradually and slowly than curvature.

4.4. Composite Ti–6Al–4V/SiC plates

Table 4 lists the thermo-mechanical properties of Ti–6Al–4V/SiC measured with samples similar to sample M8. The thermal conductivity and diffusivity were measured using the laser flash method by Holometrix (USA). The thermal expansion was measured by Ecole des Mines de Paris (France) with a dilatometer Setaram TMA 92.

Experiments on Ti–6Al–4V/SiC plates were conducted with various heat fluxes H and cooling velocities F. All curvatures were measured along the fiber direction z (longitudinal curvatures), except for sample B5, for which the long edge of the rectangle was perpendicular to the fibers, and which thus yielded curvatures along the direction y perpendicular to the fibers (transverse curvatures).

First, the composite limiting curvature was investigated and was found to differ significantly from that of unreinforced Ti–6Al–4V plates: the results showed larger scattering and the limiting curvature was reached after a longer time. Also, the limiting curvature was generally much larger than expected, whereas it was expected to be similar to the limiting curvature of unreinforced plates, because the equivalent coefficients of thermal conductivity and expansion of Table 4 are quite similar to the properties of the unreinforced alloy.

This discrepancy indicates that an additional mechanism is active in the composite plates, identified in the analysis above as the bilayer effect. Thus, as shown by Eq. (29), the limiting curvature is the sum of two contributions, i.e., the curvature due to the average temperature for a bilayer plate and the curvature due to the thermal flux. The former curvature is given by the curvature factor $\rho_{y,z}^T$ (depending whether direction y or z are considered), which represents the increase of curvature per unit temperature. The latter curvature is given by the curvature factor $\rho_{y,z}^H$, corresponding to the increase of curvature per unit flux.

To distinguish between the two types of curvatures, two main combinations of parameters H and F were examined (with $d = 47$ mm, as for the Ti–6Al–4V plates). The curvature factors were then measured as follows:

(i) The curvature factor $\rho_{y,z}^T$ was determined from the curvature ρ_1 of the plate for a small flux $H = 25$ kW m^{-2} and a cooling velocity $F = 0$. The curvature was deduced from the deflection D_1 using Eq. (33) (deflection was found to be linear with distance d, as in the case of a bimetallic strip). The limiting temperature was then about 280°C, and the convection factors h_1 and h_2 were 50 W m^{-2} K^{-1}. The measured curvature was then divided by the temperature increase of 250 K, the initial temperature being 30°C, to find the temperature curvature factor ρ^T. For those conditions, the small curvature ρ_1 found for a monolithic Ti–6Al–4V plate is negligible, and is entirely due to the small imposed flux, so that $\rho^T = 0$.

(ii) The curvature factor $\rho_{y,z}^H$ was calculated from the measurement of the deflection D_2 of the plate for a large flux $H = 200$ kW m^{-2} and a cooling velocity $F = 2.00$ m s^{-1}. The limiting temperature was then about 330°C. The convection factors were 50 W m^{-2} K^{-1} on the heated side and 620 W m^{-2} K^{-1} on the cooled side. The deflection due to this average temperature, calculated with the experimental temperature curvature factor previously determined, is subtracted from D_2 to yield D_2'. The curvature ρ_2 due solely to the thermal flux is then found by introducing this deflection D_2' into Eq. (36), because this curvature is expected to be sensitive to heat losses by the clamp in the same way as for the Ti–6Al–4V plate in Fig. 5. This curvature is then divided by the heat flux $H = 200$ kW m^{-2}, to find flux curvature factor ρ^H. For those conditions, the curvature due to the thermal flux in a monolithic Ti–6Al–4V plate is $\rho_2 = 0.18$ m^{-1}, as shown in Table 3, and the curvature factor is $\rho^H = 9 \times 10^{-7}$ m W^{-3}.

Table 5 lists the results of curvatures ρ_1 and ρ_2 together with the curvature factors for each plate. The results for ρ^T exhibit a high variability, whereas ρ^H is more constant. Flux curvature factors are slightly inferior for composites B1–B4,
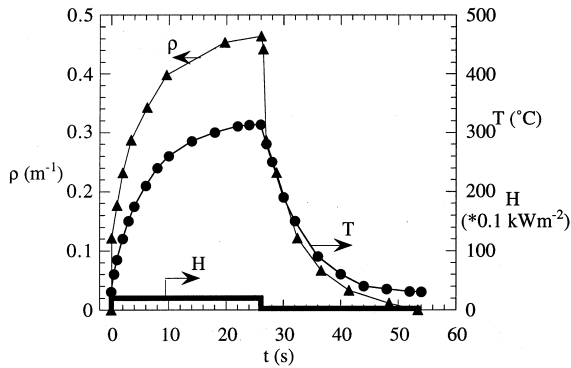
Fig. 7. Time-dependence of curvature ρ for a Ti–6Al–4V/SiC plate (sample M8) subjected to a thermal shock of 26 s duration, with a cooling velocity $F = 2.00$ m s^{-1} and a heat flux $H = 200$ kW m^{-2}.

and the curvature obtained for B5 is more pronounced than for samples B1–B4.

Fig. 7 shows the evolution of the average temperature and the plate curvature along the fiber direction as a function of time for a composite plate. For simplicity, the curvature was deduced from the deflection by using Eq. (36) as for the Ti–6Al–4V samples. The evolution differs noticeably from the case of the monolithic plates Fig. 6. In particular, the limiting curvature is reached after a much longer time. As for the Ti–6Al–4V plate in Fig. 6, the curvature is fully and rapidly recovered after the flux is interrupted, indicating again that all deformations are purely elastic.

5. Discussion

5.1. Monolithic Ti–6Al–4V plates

Table 2 lists the properties of Ti–6Al–4V needed for the calculations and Fig. 4 shows the

Table 2
Ti–6Al–4V thermal expansion α, conductivity κ and diffusivity δ at various temperatures (Boyer et al., 1994)

T (°C)	α (10^{-6} K^{-1})	κ (W m^{-1} K^{-1})	δ (10^{-6} m^2 s^{-1})
30	8.5	6.5	2.5
250	9	8.5	3.2
330	9	10	3.5
460	9.5	12	4

Table 3
Experimental (Exp) and calculated values for limiting temperature and curvature ($\bar{T}_\infty$, ρ_∞) for three combinations of heat flux H and cooling velocity F, measured for a Ti–6Al–4V plate

H (kW m^{-2})	F (m s^{-1})	$\bar{T}_\infty$ (°C)		ρ_∞ (m^{-1})	
		Exp	Eq. (7)	Exp	Eq. (23)
25	0	280	280	–	–
200	2.00	330	330	0.18	0.17
300	2.00	460	480	0.23	0.22

coefficients of convection h_1 and h_2 (h_1 equals h_2 for no cooling).

Table 3 compares experimental and calculated data, using material properties of Table 2. The limiting temperatures for fluxes $H = 25$ and 200 kW m^{-2} were used to determine convection factors. For $H = 300$ kW m^{-2}, we can compare the limiting temperature as calculated with Eq. (7) and as measured, and we find a good agreement, which confirms the accuracy of convection factors. The limiting curvatures are calculated with Eq. (23), using material properties at the corresponding temperature. A good agreement is found between experiment and prediction.

Fig. 8 compares the calculated and measured time dependence of temperature and curvature for the interval where H is non-zero. Temperature is calculated from Eq. (5) and curvature from Eq. (20), where five terms were sufficient in the sum for good convergence. Since neither equation takes into account the temperature-dependence of
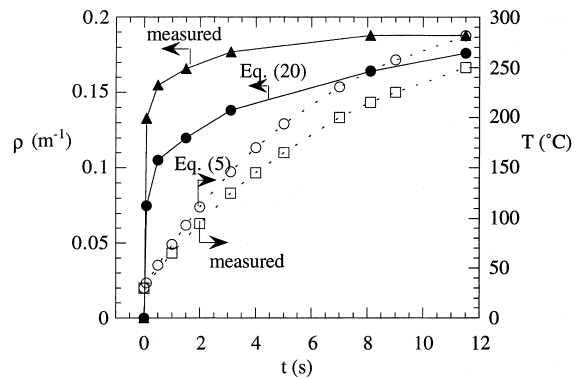

Fig. 8. Comparison between calculated and measured time-dependence of the curvature ρ and average temperature T for a Ti–6Al–4V plate subjected to a cooling velocity $F = 2.00$ m s^{-1} and a heat flux $H = 200$ kW m^{-2}.

material properties, properties of Ti–6Al–4V at 250°C given in Table 3 were used. For temperature, the match between measured and calculated data is quite good in Fig. 8. Reasons for discrepancy include difficulties of measuring a rapidly varying temperature and inaccuracies in thermal properties of the plate and coefficients of convection. The match between measured and calculated curvatures is reasonable overall, although the discrepancy in the first few seconds of the experiment is large. This discrepancy stems from various factors. First, the thermal conductivity of Ti–6Al–4V at room temperature ($\kappa = 6.5$ W m^{-1} K^{-1}) is less than the thermal conductivity at about 250°C ($\kappa = 8.5$ W m^{-1} K^{-1}) used in the calculations, thus underestimating the curvature. Second, Eq. (36) was used for the measured curvature deduced from the laser deflection, whereas heat losses might be less significant during the first seconds, where Eq. (33) could apply better, so that the measured curvature was overestimated at the beginning of the step.

Finally, after the heat flux has been stopped in Fig. 6, the temperature decreased gradually as a result of convection. The time-dependence of curvature and temperature during this phase could be analyzed in a manner very similar to that described above for the case where the heat flux is being applied. While this is beyond the scope of this article, we note that the curvature decreased very quickly, which can be explained by a rapid homogenization of temperature through the thickness of the plate, whereas the temperature decreased gradually as an effect of convection.

In conclusion, theory matches the experiments satisfactorily. It shows that Timoshenko's theory is appropriate to the kind of plate we used. The dependence of material properties is taken into account for the limiting curvatures, for which the match is quite good.

5.2. Composites Ti–6Al–4V/SiC plates

Table 4 lists the properties of Ti–6Al–4V/SiC needed for the calculations. These properties are consistent with equivalent properties as calculated with Hashin's self-consistent model (Christensen, 1979), introducing thermo-mechanical properties

Table 4
Ti–6Al–4V/SiC longitudinal and transverse thermal expansion α_z and α_y, through-thickness thermal conductivity κ and diffusivity δ at various temperatures, measured with the same composite as sample M8

T (°C)	α_z (10^{-6} K^{-1})	α_y (10^{-6} K^{-1})	κ (W m^{-1} K^{-1})	δ (10^{-6} m^2 s^{-1})
30	7	9	6.5	3.2
250	7	9	8.5	3.4
330	7	9	9	3.5

of the fibers and of the matrix. Coefficients of convection h_1 and h_2 are given in Fig. 4 (h_1 corresponds to h_2 for no cooling).

In Table 5, flux curvature factors are listed for all the composite plates. Using properties of Table 4 in Eq. (27), it is predicted to be 8×10^{-7} m W^{-3}. The discrepancy between the measured and calculated flux curvature factors can be explained by measurement errors as well as by inaccuracies in the composite equivalent properties. In particular, coefficients of thermal conductivity and expansion are difficult to determine accurately, so that thermal conductivity may have been overestimated, whereas thermal expansion may have

Table 5
Limiting curvatures of Ti–6Al–4V/SiC plates in the fiber direction[a], for a uniform temperature of 280°C (total curvature ρ_1) and for a heat flux $H = 200$ kW m^{-2} and a cooling velocity $F = 2.00$ m s^{-1} (component of curvature due solely to the thermal flux, ρ_2), temperature curvature factor ρ^T and flux curvature factor ρ^H

	ρ_1 (m^{-1})	ρ_2 (m^{-1})	ρ^T (10^{-4} m^{-1} K^{-1})	ρ^H (10^{-7} W m^{-3})
M1	0.18	0.18	6.0	9
M2	−0.05	0.18	−1.6	9
M3	0.03	0.18	1.0	9
M4	0.16	0.19	5.3	9.5
M5	0.08	0.18	2.7	9
M6	0.16	0.17	5.3	8.5
M7	0.04	0.17	1.3	8.5
M8	0.25	0.20	8.3	10
M9	0.19	0.20	6.3	10
M10	0.49	0.17	16.3	8.5
B1	0.12	0.17	4.0	8.5
B2	0.17	0.14	5.7	7
B3	0.12	0.15	4.0	7.5
B4	0.08	0.14	2.7	7
B5	0.05	0.20	1.7	10

[a] In the direction perpendicular to the fibers for sample B5.

been underestimated. That could explain why the flux curvature factor of sample M8 was measured to be 10^{-6} m W^{-1}. Besides, materials properties may vary from sample to sample, especially between M (Matra) and B (BP) samples. In spite of that discrepancy, the match is good enough to be considered as an experimental demonstration that equivalent properties can be used to determine flux curvature factors. In that regard, the measured values for ρ^H are rather homogeneous, indicating that they depend on material properties, as opposed to values for ρ^T which vary significantly between samples, because ρ^T is a characteristic of the plate itself rather than a material property. Also, the fact that ρ_y^H for sample B5 (corresponding to a transverse curvature) is larger than ρ_z^H measured for other B samples (corresponding to a longitudinal curvature) is expected since the transverse thermal expansion is larger than the longitudinal thermal expansion, as shown in Table 4. So, we believe that the mismatch between calculated and measured data can be entirely explained by the determination of composite properties and measurements inaccuracies.

In Table 6, the limiting curvature has been measured after the deflection of the laser by using Eq. (36). The calculated limiting curvature has been evaluated with Eq. (29) by using measured equivalent properties, to determine the flux curvature factor, and by using the measured temperature factor ρ^T of plate M8 (given in Table 2). Because an accurate prediction of this factor would require a very thorough and extensive observation of the composite plate, we consider it as a measured property associated to the plate, just like other thermal properties. The mismatch between the calculated and measured limiting curvature is essentially due to the mismatch for the

flux curvature factor, which has been discussed above.

To compare the time-dependence of curvature of plate M8 in the fiber direction, as measured in Fig. 7 and as predicted by Eq. (26), we use properties of Table 4 and curvature factor ρ_z^T given in Table 2. As for the monolithic material, five terms in the sum of Eq. (28) are sufficient for a very good convergence. Fig. 9 reveals a good match between the measured and calculated time-dependence of temperature and curvature, during the time where the heat flux is being applied. In particular, it shows that the increase of curvature measured in the last seconds of the thermal shock is proportional to the increase of average temperature, which validates the hypothesis that asymmetry of the fibers distribution provides a bilayer effect proportional to the increase of average temperature Eq. (26). Conversely, the curvature rises very sharply in the first seconds, in the same way as for the monolithic plate, because the function $r(t)$ given in Eq. (28) rises very sharply. We conclude that Eq. (26) provides a good model for the time-dependence of the curvature of a composite plate. The reasons for the discrepancy are multiple: difficulties of measuring a rapidly varying temperature, inaccuracies in the thermal properties of the material and in the coefficients of convection as a function of temperature, as discussed earlier.

Table 6
Experimental (Exp) and calculated values for limiting temperature and longitudinal curvature ($\bar{T}_\infty$ and $\rho_{z\infty}$) for two combinations of heat flux H and cooling velocity F, measured for a Ti–6Al–4V/SiC plate (sample M8)

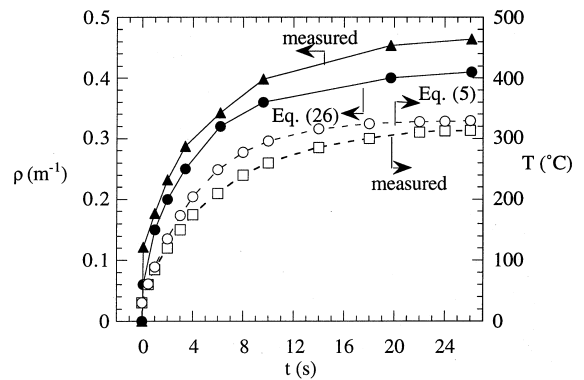| H (kW m^{-2})	F (m s^{-1})	$\bar{T}_\infty$(°C)		$\rho_{z\infty}$ (m^{-1})	
		Exp	Eq. (7)	Exp	Eq. (27)
25	0	280	280	–	–
200	2.00	330	330	0.46	0.41

Fig. 9. Comparison between calculated and measured time-dependence of the longitudinal curvature ρ and average temperature T for a Ti–6Al–4V/SiC plate (sample M8) subjected to a cooling velocity $F = 2.00$ m s^{-1} and a heat flux $H = 200$ kW m^{-2}.

As in the case of Ti–6Al–4V plates, the cooling section in Fig. 7 after interruption of the heat flux could also be analyzed in a similar manner, a task which is again beyond the scope of this article.

In conclusion, we find a good match between theory and experiment for the response of a composite plate. The results are more difficult to analyze than in the case of a monolithic plate, because of the bilayer effect which acts as an additional mechanism. However, they validate the use of equivalent properties of the composite material, together with the temperature curvature factor which can be measured separately.

6. Conclusion

Closed-form solutions are derived for the time-dependence of temperature and curvature of a monolithic plate subjected to a step-shaped heat flux and cooled by convection on both sides. The plate response can be described by an average temperature and an average thermal gradient which tend to limiting values which have been determined. The curvature of the plate also tends to a limiting value which can be simply related to the thermal flux.

The model is then extended to the case of a unidirectional composite plate with a non-uniform fiber distribution. We find that homogenized properties can be used provided that the asymmetry of the plate which leads to a bilayer effect is taken into account. Therefore, the overall curvature of such a plate is modeled as the sum of two contributions: the first curvature contribution is given by the monolithic solution with equivalent properties of the composite, while the second contribution is the result of the average temperature and is similar to the curvature of a bilayer material resulting from a change of uniform temperature.

An experimental apparatus was built to measure as a function of time the curvature and the average temperature of a plate subjected to a step-shaped heat flux. The experimental results were found to be in reasonable agreement with the theoretical analysis for both monolithic Ti–6Al–4V plates and fiber-reinforced Ti–6Al–4V/SiC plates, thus validating the model.

Appendix A

To solve the equation system (1a)–(1d) which includes non-homogeneous boundary conditions, we make a variable transformation to make it homogeneous. The temperature T is written in the form:

$$T = T^* + a + b\left(x + \frac{e}{2}\right). \tag{A.1}$$

We can check that T^* satisfies the Laplace equation Eq. (1a), and we determine the constants a and b such that T^* satisfies a homogeneous system, i.e., Eqs. (1c) and (1d) are a homogeneous system:

$$a = T_0 + H\frac{\kappa + h_2 e}{\kappa(h_1 + h_2) + h_1 h_2 e}, \tag{A.2}$$

$$b = -H\frac{h_2}{\kappa(h_1 + h_2) + h_1 h_2 e}. \tag{A.3}$$

T^* is then found in Ozisik (1993), together with the definition of the following constants:

$$\beta_m = \tan[\beta_m e]\frac{\kappa^2\beta_m^2 - h_1 h_2}{\kappa(h_1 + h_2)}, \tag{A.4}$$

$$c_m = \frac{1}{N(\beta_m)}\left[\cos[\beta_m e]\left(\frac{ah_1 - \kappa b + bh_1 e}{\kappa\beta_m}\right) - \sin[\beta_m e]\left(a + be + \frac{bh_1}{\kappa\beta_m^2}\right) - \frac{ah_1 + \kappa b}{\kappa\beta_m}\right], \tag{A.5}$$

where

$$N(\beta_m) = \frac{1}{2\kappa^2}\left[(\kappa^2\beta_m^2 + h_1^2)\left(e + \frac{\kappa h_2}{(\kappa^2\beta_m^2 + h_2^2)}\right)\right.$$
$$\left. + \kappa h_1\right].$$ (A.6)

References

Aboudi, J., Arnold, S.M., Pindera, M.-J., 1994. Response of functionally graded composites to thermal gradients. Composites Eng. 4, pp. 1–18.

Aboudi, J., Pindera, M.-J., Arnold, S.M., 1997. Microstructural optimization of functionally graded composites subjected to a thermal gradient via the coupled higher-order theory. Composites 28B, 93–108.

Boyer, R., Welsch, G., Collings, E.W., 1994. Materials Properties Handbook: Titanium Alloys. ASM International.

Christensen, R.M., 1979. Mechanics of Composite Materials. Wiley, New York.

Finot, M., Suresh, S., Bull, C., Sampath, S., 1996. Curvature changes during thermal cycling of a compositionally graded Ni-Al$_2$O$_3$ multi-layered material. Mat. Sci. Eng. A 205, 59–71.

Finot, M., Suresh, S., 1996. Small and large deformation of thick and thin-film multi-layers: effects of layer geometry, plasticity and compositional gradients. J. Mech. Phys. Solids 44, 683–721.

Mukherjee, N., Sinha, P.K., 1996. Thermal shocks in composite plates: a coupled thermoelastic finite element analysis. Composite Structures 34, 1–12.

Ozisik, M.N., 1993. Heat Conduction, 2nd ed. Wiley, New York.

Stoney, G.G., 1909. The tension of metallic films deposited by electrolysis. Proc. Roy. Soc. Lond. Ser. A 82, 172–175.

Suresh, S., Giannakopoulos, A.E., Olsson, M., 1994. Elasto-plastic analysis of thermal cycling: layered materials with sharp interfaces. J. Mech. Phys. Solids 42, 979–1018.

Timoshenko, S.P., Goodier, J.N., 1970. Theory of Elasticity, 3rd ed. McGraw-Hill, New York.

Timoshenko, S.P., Woinowsky-krieger, S., 1959. Theory of Plates and Shells. McGraw-Hill, New York.